Manuscript submitted to: Volume 2, Issue 2, 219-244.

AIMS Biophysics DOI: 10.3934/biophy.2015.2.219

Received date 18 February 2015, Accepted date 15 June 2015, Published date 22 June 2015

Review

Single-particle based helical reconstruction—how to make the most of real and Fourier space

Carsten Sachse

EMBL—European Molecular Biology Laboratory, Structural and Computational Biology Unit, Meyerhofstr. 1, 69117 Heidelberg, Germany; Email: carsten.sachse@embl.de.

Abstract: The helical assembly is a fundamental organization principle of biomacromolecules. To determine the structures of helical filaments or tubes has been helped by the fact that many different views of the helical unit are present to reconstruct a three-dimensional image from a single helix. In this review, I present the current state of helical image reconstruction from electron cryo-micrographs by introducing Fourier-based processing alongside real-space approaches. Based on this foundation, I describe how they can be applied to determine the symmetry and high-resolution structure of helical assemblies. In the past, the main structure determination approach of helical assemblies from electron micrographs was the Fourier-Bessel method, which is based on a comprehensive theory and has generated many successful applications in the last 40 years. The emergence of the single-particle technique allowed segmented helical specimens to be treated as single particles, thus rendering new specimens amenable to 3D helical reconstruction and facilitating high-resolution structure analysis. However, helical symmetry determination remains the crucial step for a successful 3D reconstruction. Depending on the helical specimen, Fourier and real-space approaches or a combination of both provide important clues to establish the correct helical symmetry. I discuss recent developments in combining traditional Fourier-Bessel procedures with single-particle algorithms to provide a versatile and comprehensive approach to structure determination of helical specimens. Upon introduction of direct electron detectors, a series of near-atomic resolution structures from helical assemblies have become available. As helical organization is fundamental to many structural assemblies of the cell, these approaches to structure elucidation open up promising capabilities to study the underlying structures at atomistic resolution.

Keywords: Helical assemblies; Fourier Bessel reconstruction; layer lines; single-particle helical reconstruction; high-resolution electron cryo-microscopy; direct electron detectors

1. Introduction

The first three-dimensional (3D) image reconstruction from electron micrographs was obtained from the helical tail of bacteriophage T4 [1]. Prior to these reports, analysis of X-ray diffraction patterns of DNA fibers led to the development of helical diffraction theory formulated independently by Cochran, Crick, Vand [2] and Stokes (unpublished). Subsequently, two-dimensional (2D) Fourier Bessel analysis was applied to X-ray fiber diffractograms of tobacco mosaic virus (TMV) and paved the way for elucidating the architecture of helical protein assemblies [3,4]. The fact that a single helical assembly can contain thousands of unique views of the repeating molecular unit provides an ideal approach to overcome the poor signal-to-noise ratio encountered in images from electron microscopy (EM). Indeed, studies on helical assemblies [1] formed the basis for further development of 3D EM techniques, for instance by exploiting different symmetries present in icosahedral viruses [5]. Further advances in molecule preservation by plunge-freezing them in liquid ethane formed the foundation for high-resolution analysis of large biomacromolecules [6]. The first near-atomic resolution insights from electron cryo-microscopy in vitreous ice were obtained from 2D crystals of bacteriorhodopsin [7]. Helical arrays can be understood as 2D crystals by converting the cylinder surface into a flat sheet. Further improvement and expansion of Fourier-based helical reconstruction yielded the first near-atomic resolution structures of helical assemblies of the flagellar filament and the tubular nicotinic acetylcholine receptor became available [8,9].

As many molecules resist the formation of continuous and regular arrays, image analysis of molecules without any symmetry has become a major focus of development in the 3D EM field. The so-called single particles do not occur in repetitive arrangements but are monodispersely distributed over the EM grid as if being in solution. Noisy images of molecules embedded in negative stain were used to classify views and orientations [10] and, later on, to determine the molecular shape of ribosomes by iterative projection matching [11]. According to the EM databank [12], the single-particle technique has become the dominant discipline in cryo-EM structure determination as it does not require the molecule to form a crystal or a symmetrical arrangement. At the same time, icosahedral and helical assemblies greatly benefited from the application of the single-particle methodology as a series of near-atomic resolution structures were obtained [13–15]. Subsequently, smaller megadalton complexes with point group symmetry such as chaperonin TRiC were determined at comparable resolution [16]. Following the introduction of new hardware, i.e. direct electron detectors devices (DDD), signal-to-noise ratio of the molecular images significantly improved and frame acquisition enabled movement tracking of molecules during the imaging. As a result, a series of atomic-resolution structures of large asymmetric ribosomes [17,18] and 700 kDa 20S proteasomes [19] became available recently. In addition, even smaller asymmetric molecules less than 200 kDa have become within reach of near-atomic resolution [20]. The acquisition of cryo-micrographs using novel DDDs has also significantly improved the quality of images from helical assemblies. Current examples include 3D structures of CARD domain filaments at 3.7 Å resolution [21], ParM filaments at 4.3 Å resolution [22], the F-actin tropomyosin complex at 3.8 Å [23] and TMV at 3.35 Å resolution [24].

Recent hardware developments are redefining the role of 3D cryo-EM in structural biology. In addition, powerful single-particle based structure determination software has been developed for analysis of helical assemblies [25–29] all of which apply single-particle algorithms while exploiting helical symmetry. In all of these approaches, the main challenge remains the determination of initial

helical symmetry parameters before those algorithms can be applied. In the present review, I provide an overview of the various types of helical assemblies, the characteristics of real-space and Fourier space methods that exist for helical symmetry determination, as well as possible ways to combine these different approaches with the aim of reconstructing high-resolution 3D structures of these assemblies.

1.1. Helical assemblies: From filaments to tubes

A helical assembly constitutes a set of repetitive molecular units to which transformations in location and orientation according to helical parameters rise z and helical rotation φ around a central helical axis have been applied (Figure 1) [30]. An equivalent and useful presentation of helical symmetry is the pitch P and number of units per turn N, which corresponds to the ratio of number of units u divided by number of turns t over an exact repeat distance c:

$$N = u/t \qquad (1)$$

For example, in the case of TMV the repeat distance c is 69 Å, which corresponds to 49 subunits that revolve 3 times around the helical axis, i.e. number of units per turn N equals 49/3 or 16.34. The conversion of z and φ (rise, rotation) to P and N (pitch, number of units per turn) convention is obtained as follows:

$$N = 360°/\varphi \qquad (2)$$

$$P = z*N \qquad (3)$$

A summary of the variables used throughout the manuscript can be found in Table 1.

Table 1. Summary of variables required for description of helical symmetry in real and in Fourier space.

Variable	Symbol
Helical rise (Å)	z
Helical rotation (º)	φ
Pitch (Å)	P
Number of units per turn	N
Repeat distance (Å)	c
Number of units	u
Number of turns	t
Rotational symmetry	n-fold
Layer line height (1/Å)	h
Layer line number	l
Bessel order	v
Helical radius (Å)	r
Reciprocal radius (1/Å)	R

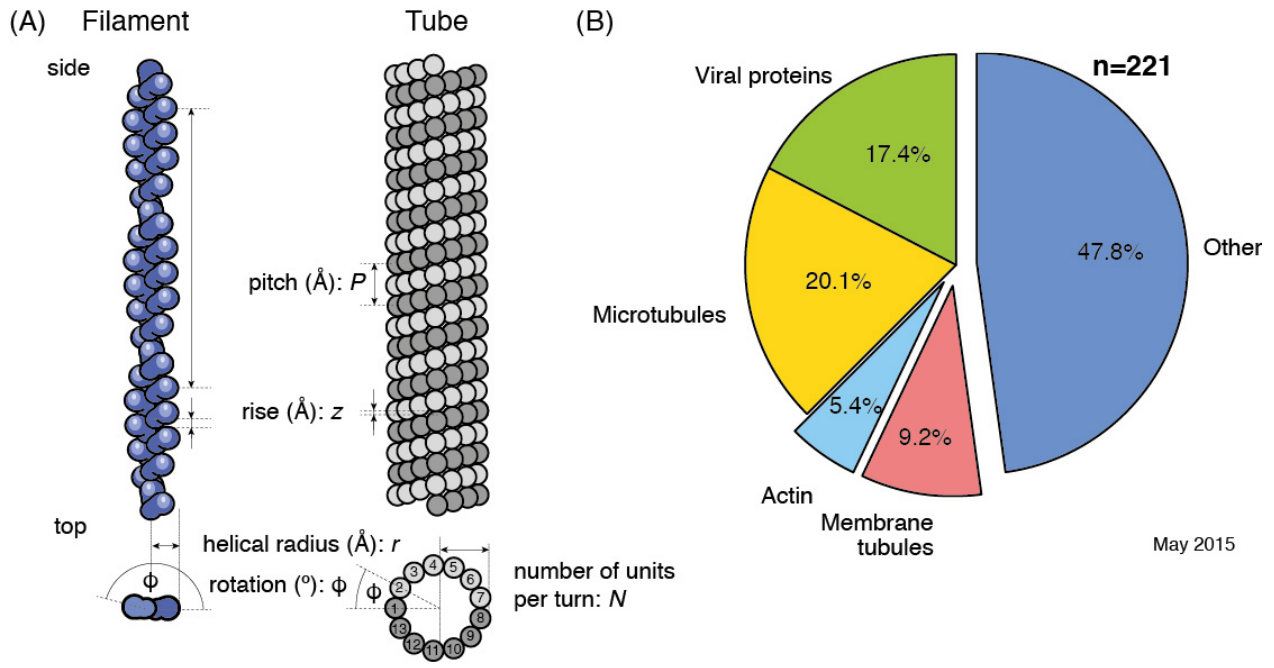

Figure 1. Main properties of helical assemblies and the most common helical entries of the EM databank. (A) Left. Filaments are thin elongated assemblies. The main subunit interactions are found at the center of the filament and between units above and below (side view). Right. Tubular assemblies often have wider helical radii than filaments and possess a hollow center (top view). The main interactions are stabilized between adjacent units from all sides of the helical lattice. All of these assemblies have in common that one helical unit can be repeated by a helical rise *z* and rotation *φ* transformation. Helical symmetry can be equivalently expressed as the pitch *P* and the number of units per turn *N* (equations (2) and (3)). The molecular units of the helical assembly are located at helical radius *r*. (B) According to the 221 helical entries from the EM databank, the best-studied assemblies include viral proteins, microtubules, actin and membrane tubules, which together make up approximately half of the entries.

The helical assembly is fixed in three dimensions such that each unit is stabilized by the same biochemical environment [31]. In principle, two forms of such an assembly are known. If the asymmetric unit is located close to or on the helical axis the resulting assembly is thread-like as in actin filaments [32]. In the case when the helical units have an offset position from the helical axis with a hollow center, they form a tubular assembly as in microtubules or TMV [33,34]. A distinct feature of tubular assemblies is that each repeating unit is stabilized by multiple neighboring subunits from the surrounding helical lattice, thus conferring stability to form rigid and straight tubes with high persistence lengths. This is in contrast to thinner filaments that are mainly stabilized by interactions to the units above and below. Additional examples of biological filamentous assemblies include sickle-cell fibers and amyloid fibrils [35,36]. Moreover, membrane proteins are known to form tubular membrane arrays, e.g. TSPO, nicotinic acetyl choline receptor and Ca^{2+}-ATPases [8,37,38]. The cell harbors many more types of helical assemblies that are involved in very diverse processes such as viral infection, innate immune and signaling response [21,39]. Based

on the depositions of a total of 221 helical structures in the EM databank (EMDB) [12], microtubules, actin, membrane tubules and viral assemblies belong to the best studied helical specimens (Figure 1B). Many structures of actin and microtubules alone and in complex with binding partners are available and they make up more than a quarter of helical entries in the EMDB. More recently, due to hardware improvements, near-atomic resolution structures of actin and microtubules have become available, thus underlining the importance and great scientific interest in these helical assemblies [40,41].

In order to determine the *de novo* 3D structure of helical specimens, the symmetry determination is the critical step of the structure determination procedure. The helical parameters can be obtained by traditional methods based on the analysis of the Fourier spectra of helices (Figure 2A). More recently real-space approaches have been successfully applied (Figure 2B). Subsequently, helical symmetry refinement can be performed simultaneously or independently (Figure 2C) of the iterative helical reconstruction procedure to yield the final high-resolution structure (Figure 2D).

1.2. Helical symmetry in real space and Fourier space

In analogy to diffraction spots from 2D crystals, projection images of helices converted to Fourier space contain a pattern of structure factor peaks as streaked reflections termed layer lines (Figure 3A–C). The vertical axis of the transform is referred to as the meridian and the horizontal axis termed equator. Diffraction patterns of helices, however, contain contributions from two separate lattices: first, the lattice of the front or the near side of the helix facing the observer and, second, the lattice of the back or the far side of the helix (Figure 3D–F). Each of these lattices gives rise to a set of corresponding layer lines in the Fourier transform, which are mirror symmetric along the meridian (Figure 3G).

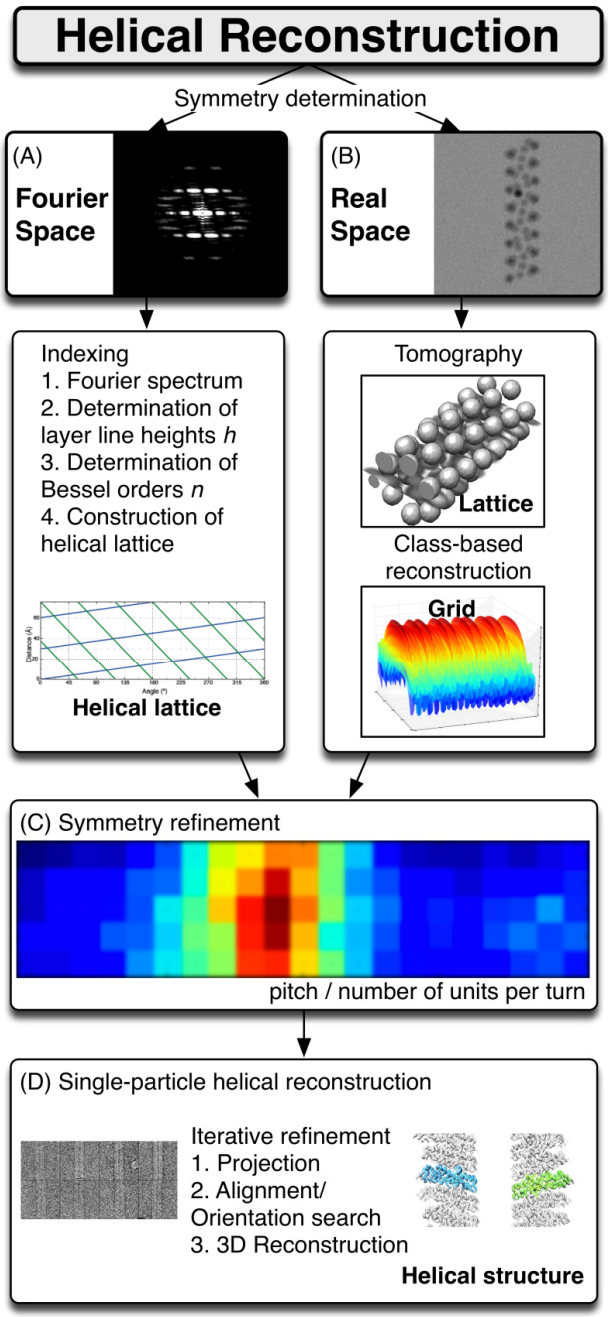

Figure 2. Flow chart of helical reconstruction including symmetry determination in Fourier and real-space and single-particle structure determination. (A) Fourier spectra provide important clues for helical symmetry determination. Indexing of Fourier spectra from helices yield helical lattice parameters. (B) Alternative approaches exist in real space such as sub-volume averaging from tomograms and class-based helical reconstruction. (C) The determined lattice parameters are refined by performing a grid search over symmetry combinations that are evaluated by amplitude correlation of power spectra. (D) The refined symmetry parameters are required to correctly impose helical symmetry while performing iterative single-particle structure refinement.

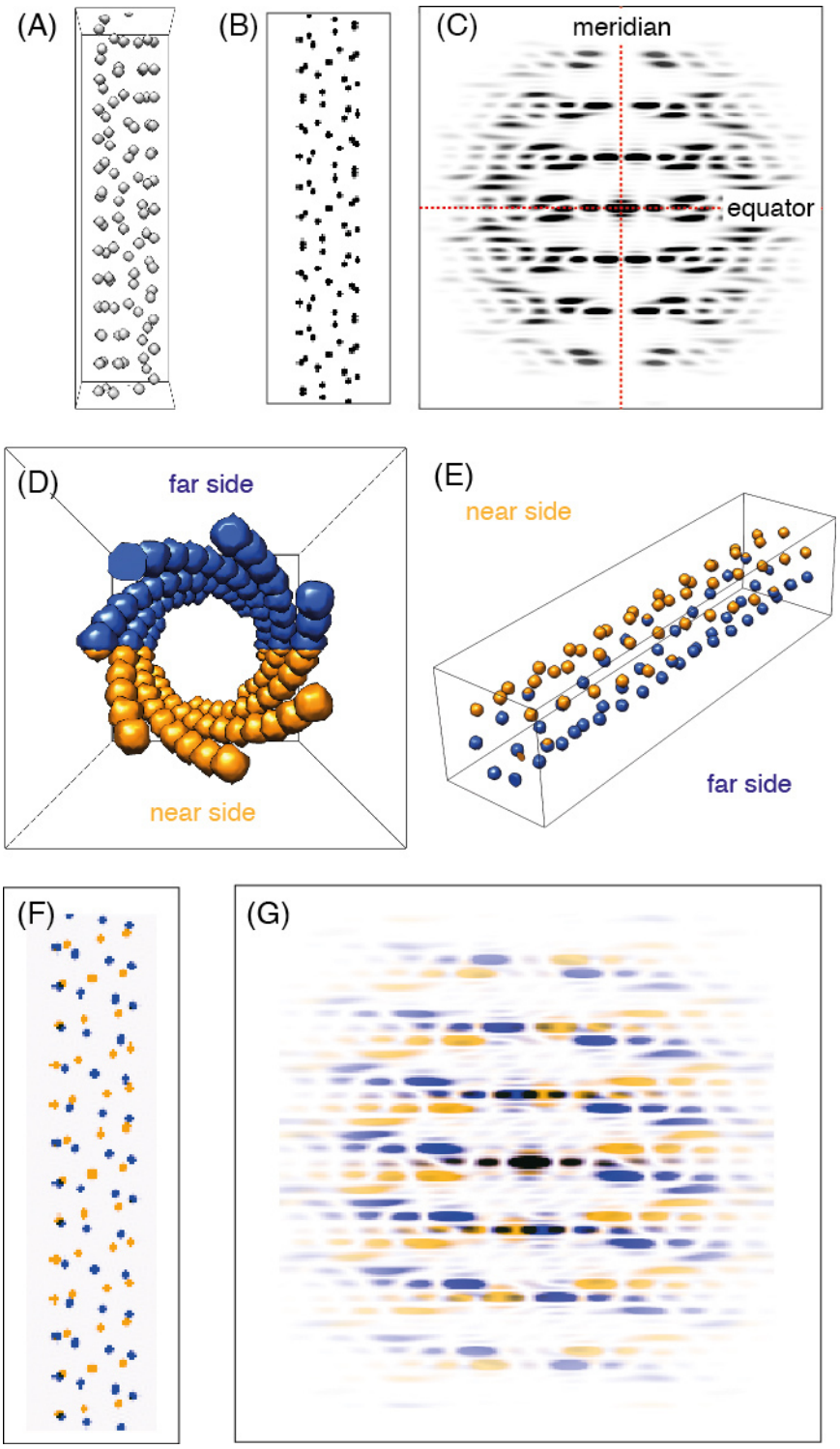

Figure 3. Helical lattice and diffraction pattern. (A) Side view of helix. (B) Helical projection and (C) corresponding 2D Fourier transform consisting of a pattern of stacked layer lines. The vertical axis and horizontal axis are referred to as meridian and equator. (D) Top and (E) side view of helix with colored near (orange) and far (blue) side. (F) Composite helical projection from near (orange) and far (blue) side of the helical lattice. (E) Composite diffraction pattern with near (orange) and far-side (blue) contributing layer lines.

Each layer line is mathematically derived from a Bessel function and represents a periodic wave that repeats v times around the circumference of a cylinder. Since a helical wave must revolve an integral number of times around a closed cylinder surface, v is confined to integer values [42]. A molecular helical assembly can be decomposed into sets of such helical waves. This concept was used to extract the corresponding layer line components in Fourier space and compute 3D reconstructions of helical specimens [1,43]. The interpretation of the diffraction pattern is accomplished by decomposing the spectrum into a set of assigned layer line components. This process is also known as indexing the helical diffraction pattern and is the crucial step for *de novo* structure determination of helical assemblies. The amplitudes of the Fourier transform are almost identical for all azimuthal views of a helix, whereas the phases vary. Layer lines are found aligned perpendicularly to the meridian and spaced apart by the reciprocal distance of the helical repeat c. Mathematically, the lines are described by oscillating Bessel functions $J_v(X)$ with discrete orders v (Figure 4A) that depend on the helical radius r and the reciprocal radius R from the meridian (Figure 4B):

$$J_v(2\pi * R * r) \qquad (4)$$

According to Figure 4C peaks from layer lines of small Bessel order v are located close to the meridian as opposed to large Bessel orders that are spaced further away from the meridian and possess decreasing peak maxima. Each layer line has a horizontal position in the Fourier spectrum, which is described by the layer line height h or the layer line number l. Once the layer lines have been assigned with their layer line heights h and order v, a real-space lattice can be derived from the intersections of the layer line waves, which defines the unit positions of the helical array. In experimental EM images that contain noise and dampened high-resolution information transfer, layer lines with large meridional distances from the origin and high orders are very difficult or impossible to index in the diffraction pattern. Therefore, depending on how discrete layer lines are distributed in the Fourier spectrum indexing may not be possible from such projection images alone. An extreme example of such an array are the molecular ribbons of amyloid fibrils, which exhibit a very low resolution pitch or crossover distance at 1500 Å and very high resolution features at 4.8 Å of the β-strand distance [35], i.e. a particular combination rendering Fourier-based reconstruction impossible. An additional limitation in interpreting the Fourier spectra from helical projections is that multiple layer lines can coincide onto the same pixel [44]. When two different layer lines are too close in Fourier space due to discrete pixel sampling, they overlap and are impossible to correctly assign. Despite the known shortcomings, Fourier spectra provide rich and condensed information about the 3D organization of helical arrays and should be used as the first point of reference.

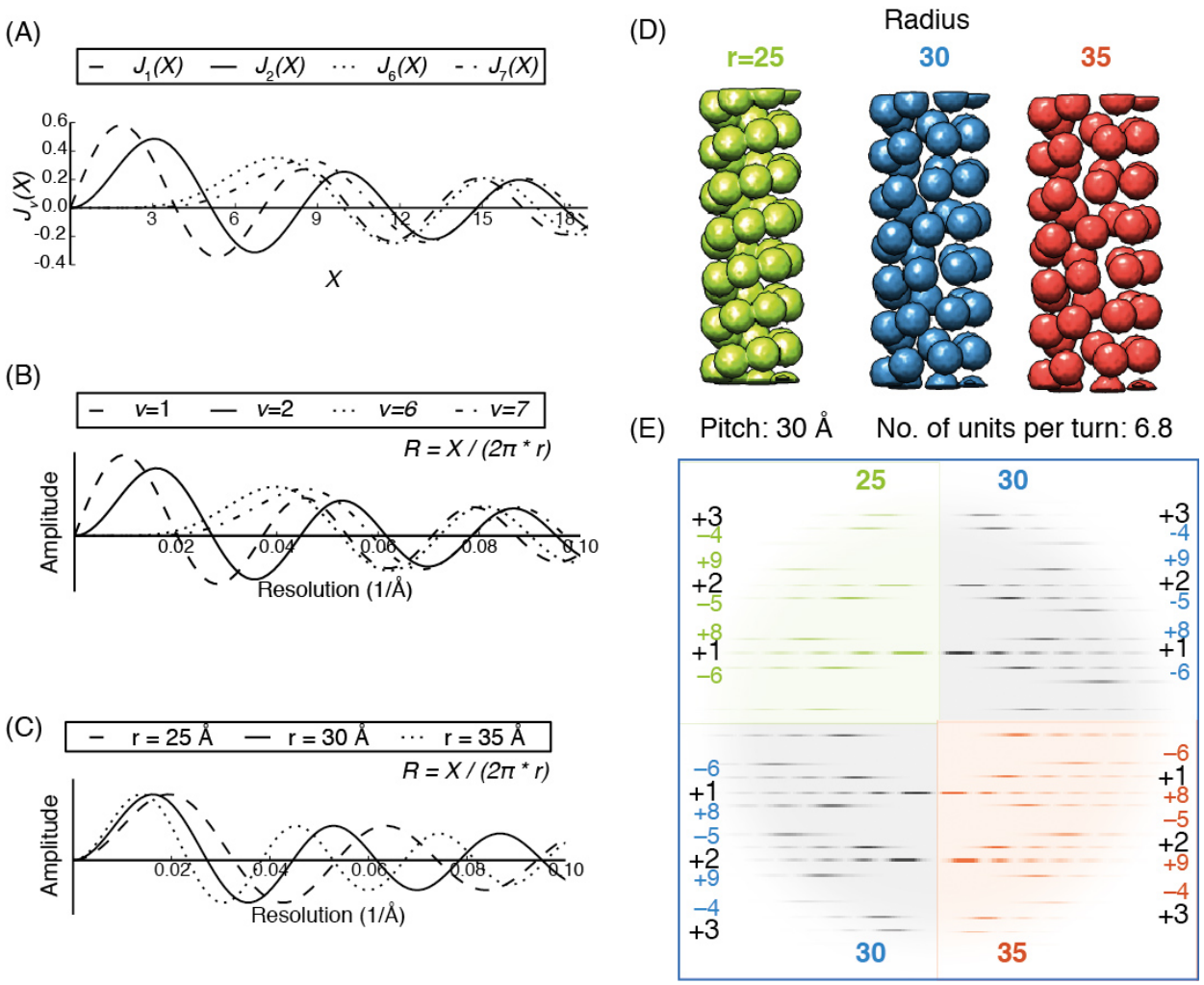

Figure 4. Layer lines are derived from Bessel functions that depend on the order and the helical radius. (A) Standard Bessel functions J_v of orders v = 1, 2, 6, 7. (B) Layer line amplitudes derived from Bessel functions of orders v = 1, 2, 6, 7 plotted as a function of resolution from the meridian assuming a helical radius of 30 Å. (C) Peak positions of layer line amplitudes of Bessel order v = 2 move closer to the meridian with increasing helical radii of r = 25, 30, 35 Å. (D) Example of 3 helices that share helical symmetry but vary in helical radius of r = 25, 30, 35 Å. (E) Theoretical Fourier spectra comparison merged 3 tiles of the above helices into one Fourier spectrum reveal that the layer line peak distance from the meridian decrease reciprocally to the increase of the helical radius. Corresponding Bessel orders of layer lines are listed at the left and right side of the spectrum.

1.3. Fourier approaches to determine helical symmetries

The simplest approach to examine the projection image of a helical structure is to crop an elongated rectangular box encompassing a long and straight helix, add mean density around the helix and compute the Fourier spectrum [45,46]. To overcome limited sampling of the layer lines in Fourier space, the images are often padded with the average density value around the central filament

by 3 times the image dimension, so that the amplitudes are interpolated and layer lines better separated from each other. Thus, layer line heights can be measured and their corresponding orders can be assigned. Many helical assemblies, however, are not perfectly straight, they may be tilted out of the ice layer or their projections suffer from imaging imperfections or defocus modulation by the contrast-transfer-function (CTF) of the microscope. Ideally, the indexing procedure uses straight helices to maximize the resolution of detectable layer lines, which can be achieved by stringent selection from many micrographs. In more recent protocols, segmented helices are treated as strings of single particles [27,47]. Examination of averaged Fourier or power spectra from segmented helices can effectively reduce the impact of long-range distortions of the helix and has the advantage that many helices can be combined to yield improved signal-to-noise spectra. The analysis of such an averaged amplitude spectrum can provide most of the required information for pattern indexing with little computational effort. It should be noted, however, that upon averaging power spectra phase information is lost. In order to conserve phase information, it is required to average the same helical views by single-particle based classification methods in real space [27,48,49]. Once such class averages are available, they effectively yield improved signal images and after conversion to Fourier space contain accurate amplitude and phase information that is ideally suited for the indexing procedure.

Indexing the diffraction pattern is the key step to determine helical symmetry. As excellent and more extensive reviews are given elsewhere [42,44,50], I will only briefly summarize the essential steps of the procedure. First, layer line heights h are to be measured. Preferably sharp layer lines with low Bessel order v close to the meridian should be examined first and assigned. Second, their meridional distance is to be measured and the corresponding Bessel order v determined by taking the helical radius r obtained from real-space analysis into account (equation (4)) [42]. In addition, the phase difference from opposite sides of a layer line helps to discriminate whether the corresponding Bessel orders v are odd or even [50]. For more details on the properties of phase differences, refer to the discussion about the effect of out-of-plane tilt in section 1.4 and Figure 6. It should be added that the hand of the corresponding helical waves cannot be determined from helical projection images and require additional data or external information (see below). The intersections of the corresponding helical waves can be directly converted into the rise/rotation or pitch/unit number parameter convention. Using these parameters, the layer lines selection rule can be used to test whether the predicted layer lines agree with the observed ones and whether the observed ones have been indexed correctly [2].

1.4. Ambiguities and potential confounders of the Fourier symmetry determination procedure

Despite the fact that the theory of the indexing procedure of the layer lines is well established, there are a number of practical complications that arise from indexing of biomolecular helices in projection images taken in the electron microscope. First, biological helical assemblies are built from units containing 100 s to 1000 s of atoms having a range of helical radii r that contribute to a range of possible meridional peak distances (Figure 4D/E). Second, EM samples are imaged under focus and therefore the images suffer from modulation of the Fourier amplitudes [51], which in turn affects the amplitude and position of peaks on the layer lines and adds uncertainty to the peak determination. Although this limitation can be alleviated by averaging multiple Fourier spectra taken at different defoci, an amplitude modulation often remains present in particular at low resolution frequencies.

Third, helices embedded in ice do not always lie perfectly in the image plane but exhibit slight out-of-plane tilt that leads to deviation of amplitudes and phases from the ideal helix (see below). Fourth, EM images taken in vitreous ice suffer from high-resolution amplitude decay [52]. All of the abovementioned problems are true for perfectly built helical assemblies but in practice many helical architectures are substantially flexible and the helical order is not perfectly maintained up to high resolution. A comprehensive overview of the effects of distortions on helical structures is given by DeRosier [53]. As a result, only a small number of layer lines at low resolution and with low Bessel orders v can be reliably indexed. All of the above facts add uncertainty to the determination of the Bessel orders, which would otherwise be a precise procedure.

Consequently, ambiguities in the layer line indexing procedure can arise as there are equivalent combinations of layer line Bessel order solutions available, which either completely match the observed pattern or are very similar. In order to derive the relationships of such ambiguities, it is useful to consider the helical symmetry parameters in pitch P and number of units per turn N, which is an equivalent notation to helical rise z and rotation φ (equations (2) and (3)). Ambiguous Fourier spectra arise from helices with identical pitches P but with number of units per turn N' related by:

$$N' = 2 * k + f \qquad (5)$$

and

$$N' = 2 * k - f \qquad (6)$$

where k is integer and f represents the distance ($0 < f < 1$) of N to the closest multiple of 2 (Figure 5A) [27].

Let us consider 3 helices that share the helical pitch P = 30 Å but vary in number of units per turn N = 6.8, 7.2, 8.8, respectively. Here, k = 3 and f = 0.8 yield N = 6.8 and k = 4 to yield N' of 7.2 and 8.8. For illustration purposes, we keep the helical radius constant to better explore the slight differences in layer line orders. While low-resolution layer lines with low Bessel order remain identical, only higher order layer lines vary (Figure 5B). It is important to bear in mind that the same variation can also be caused by varying density features at different radii (Figure 4C/E). In 3D structure refinements, when symmetry is imposed, density features at the corresponding radii are enhanced by symmetry averaging and re-projected Fourier spectra of that incorrect structure will still be identical to the Fourier spectra from the images [27,54]. Therefore, the same helical projections can be generated from different but related 3D helices. This relationship will hold for solutions of integers that are close to each other, whereas it breaks down when the difference in layer line orders cannot be compensated by helical radii anymore. To clarify those ambiguities, all of the 3D image reconstructions should be computed by imposing the related symmetries. Only one of the 3D reconstructions will be correct, which will be the one revealing high-resolution structural features compatible with secondary structure and/or side-chain densities known from the respective protein. Ambiguous Fourier spectra arise from related number of units per turn and equal pitch helices.

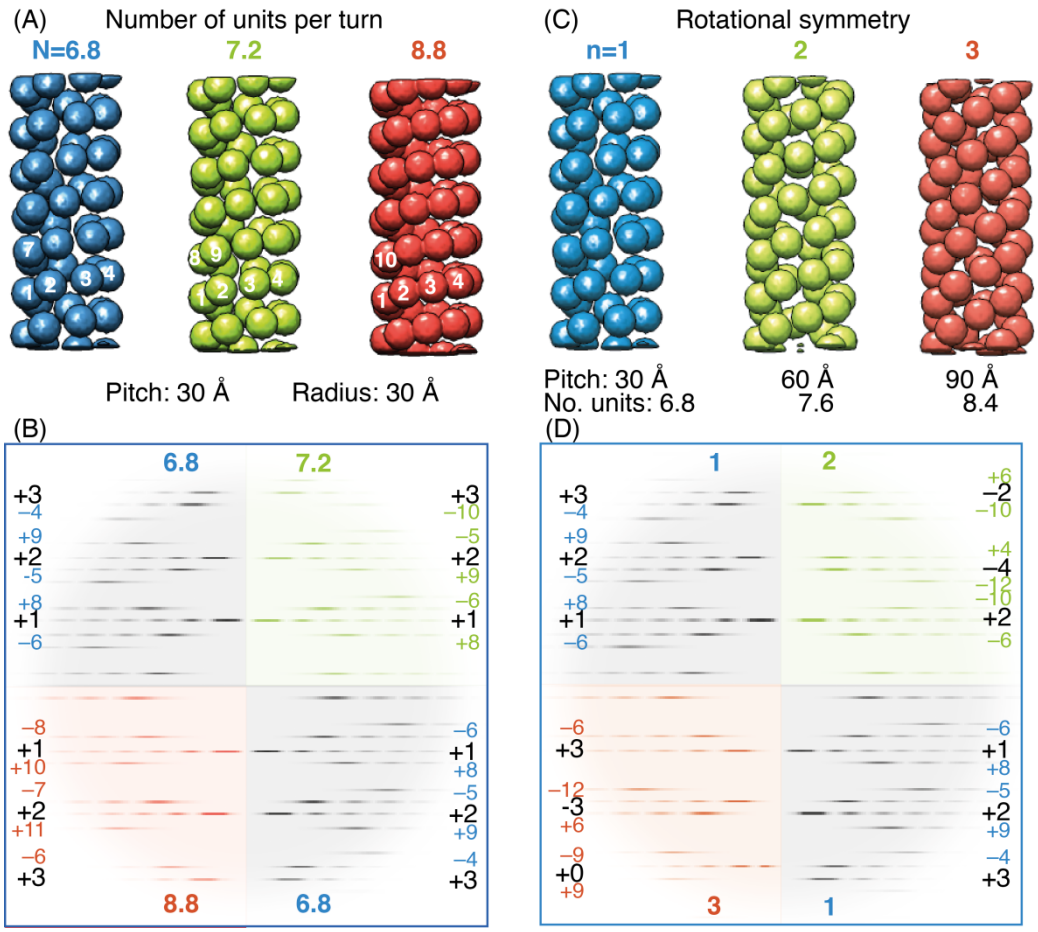

Figure 5. Ambiguities and confounders in Fourier spectra of helical model projections. (A) Related helical diffraction patterns are obtained from modeled helices that share the same pitch *P* but are related in their number of units per turn *N*. Example of 3 helices that share the same pitch but differ in their number of units per turn *N* = 6.8, 7.2, 8.8. (B) The interpretation of a real biological helix built from many atoms is complicated by the combined effects of number of units per turn and the radius of the helical feature observed in the Fourier spectrum. For purpose of illustration, we keep the helical radius constant at 30 Å in order to make the spectra presented here distinguishable from each other. Theoretical Fourier spectra comparison merged from 3 respective tiles based on a constant helical radius of 30 Å. Corresponding Bessel orders of layer lines are listed at the left and right side of the spectrum. While the lower-order layer lines share the identical Bessel orders, higher-order layer lines vary in their precise composition. (C) Very similar Fourier spectra are obtained from helices that possess *n*-fold rotational symmetry, where their pitch *P* is a multiple of n and number of units per turn *N* are related. 3 helices vary in their number of units per turn *N* = 6.8, 7.6, 8.4 and have additional rotational symmetry *n* = 1, 2, 3. (D) Theoretical Fourier spectra merged from 3 respective tiles show that the layer line heights remain identical whereas the respective Bessel orders vary significantly in their low and high orders.

The set of Fourier spectra prone to misinterpretation requires extension when, in addition to helical symmetry, point group symmetries are taken into account. In analogy to single particles, cyclic or *n*-fold rotational symmetry around the helical axis or an additional dyad symmetry perpendicular to the helical axis may be considered [55]. In the presence of *n*-fold rotational symmetry, Bessel orders *v* that are not multiples of *n*-fold will be cancelled and not be present in the helical diffraction pattern [30]. As a consequence, similar Fourier spectra with the following symmetries can occur, which share the same layer lines heights. A helix with pitch *P* and number of units per turn *N* has similar Fourier patterns to helices of *P'* and *N'* with *n*-fold rotational symmetry (*n* is integer):

$$P' = n * P \qquad (7)$$

$$N' = n * (k + f) \qquad (8)$$

and

$$N' = n * (k - f) \qquad (9)$$

where *k* is the integer that is the closest multiple of *n* to *N* and f the corresponding fractional part ($0 < f < 0.5$).

For example, Fourier spectra of 3 helices are similar in rotational symmetries n = 1, 2, 3, pitches P = 30, 60, 90 Å and N = 6.8, 7.4, 8.2 (Figure 5C/D). In these cases, when k = 7, 4, 3 and f = 0.2 according to equation (9), they yield the respective values of *N*. Despite the fact that the layer lines share the same position they vary significantly in their respective low and high orders. In that aspect they differ from the truly ambiguous solutions illustrated above as they are different. Helices share similar Fourier spectra with helices of *n*-fold rotational symmetry when the pitch *P* and number of units per turn *N* is related by multiples of *n*.

In experimental EM images, out-of-plane tilt modulates the amplitudes and phases of the Fourier transform of helices and therefore complicates the indexing procedure [56]. In order to rationalize the out-of-plane tilt effect, it is helpful to envisage the 3D Fourier transform of a helix (Figure 6A), which is made up of parallel layer planes. In an ideal in-plane projection (Figure 6B), the observed helical diffraction pattern (Figure 6C) corresponds directly to the central section of the 3D Fourier transform. In addition, phase differences computed between opposite sides of layer line profiles reveal the parity of the Bessel order. When phase differences are around 0º, the Bessel order of that layer line is even whereas phase differences of 180º indicate that the layer line is of odd Bessel order (Figure 6D). As many helical specimens are recorded slightly out of the image plane, the extracted section of the 3D transform will be tilted and thus layer-line heights, peak densities and phase differences deviate from the properties of ideal helical waves discussed above (Figure 6E–H). The changes on the image induced by out-of-plane tilt increase with the distance from the equator thus the resolution of the respective layer lines. Despite the fact that out-of-plane tilts commonly follow a Gaussian distribution [13], they can either be unintentionally induced by the carbon film [57] or by preferred orientation of the specimen out of the ice plane. The effect of helices imaged out of plane adds uncertainty to the interpretation of the observed layer lines and finally to the indexing procedure as a whole.

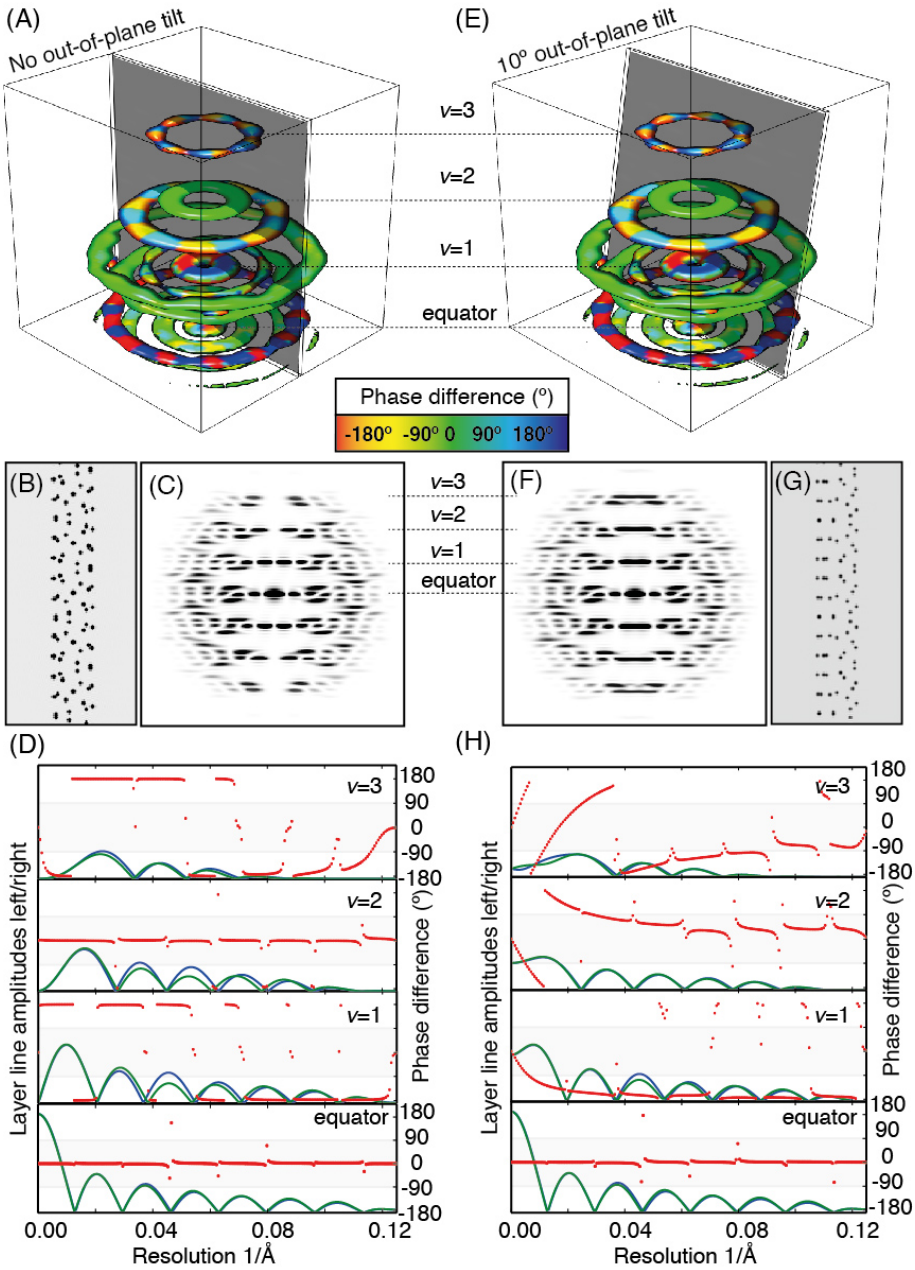

Figure 6. Effect of out-of-plane tilt of the specimen on helical diffraction patterns. (A) 3D Fourier transform of a helix consists of planes of rings corresponding to layer line peaks from 2D transforms. Phase differences are superimposed onto isosurface display in rainbow color scheme (red to blue; −180º to 180º). (B) Ideal helical projection when helix is in image plane. (C) Fourier spectrum of no out-of-plane projection. (D) Amplitudes of equator and layer lines with Bessel orders *v* = 1, 2, 3 (green, blue), phase differences between opposite sides of meridian (red). Odd Bessel orders have phase differences of 180º whereas even Bessel order layer lines display phase difference around 0º. When the specimen is imaged in plane the power spectrum of the helical projection coincides with the central section in Fourier space. (E) Whereas when the specimen is tilted out of the plane the helical power spectrum corresponds to the tilted section in the 3D Fourier

Transform. (F) Helical Fourier spectrum and (G) corresponding projection. (H) Amplitudes of layer line and corresponding phase differences. At higher resolution layer line peaks broaden and density shifts towards the meridian. Phase differences deviate from ideal 180º or 0º for odd and even Bessel orders.

An additional dyad axis that runs perpendicularly to the helix will not affect the Fourier spectrum as it does not change the helical lattice [58]. Therefore, it does not need to be treated here as a case that is prone to misinterpretation. In conclusion, ambiguous Fourier spectra can arise from parameters of constant pitches *P* and related number of units per turn *N*, and similar Fourier spectra can occur from helices where *n*-fold rotational symmetry is present, and their pitches are related by multiples of *n* and corresponding number of units per turn. These simple relationships should be kept in mind when indexing layer lines. When ambiguities remain unresolved from this procedure or a high-resolution reconstruction is not possible, it is essential to apply additional approaches that provide independent information such as electron tomography as detailed below (Figure 2B) or that provide complementary information such as mass measurements by scanning transmission electron microscopy (STEM).

1.5. Real-space approaches for symmetry determination

Given the complications that can arise from the interpretation in the Fourier domain, additional attempts have been made to analyze and determine symmetries in the real-space domain. Gross morphological features, such as helical radius or helix projections, that sum the image density along the helix are important to be analyzed and may reveal important architectural features of the helix. For example, when the information content of Fourier analysis is limited, measurements of crossover, pitch or half-pitch distances in real space can provide important clues on helical parameters [59]. An additional advantage of helices is that a single image already provides many views of the helical unit. To make use of that property, single-view class averages can be used to reconstruct 3D structures [27]. In such a case, artifacts in class averages arising from overlapping segments should be avoided by randomizing the step between segments. The advantage of class-based helical reconstruction is that it is computationally highly parallelizable so that many structures from a large array of symmetry combinations can be generated. The resulting 3D structures can be re-projected and compared with the starting class average. As a result of such an analysis, those helical parameters corresponding to the ambiguous relationships mentioned above will exhibit high similarity scores. This approach is potentially powerful and easy to integrate into a single-particle processing workflow, but it relies on accurate class presentations of the helix, which can be difficult to obtain for certain helices. Real-space analysis reveals that ambiguous relationships persist between certain helical symmetries in the image domain and need to be considered when combining 2D helical projections to 3D helical structures.

Sub-volume averaging from electron tomograms represents a different approach to determine the initial helical symmetry parameters. In contrast to previously discussed approaches, it does not rely on interpreting 2D helical projection images. Typically, a series of low-dose images from the sample under different tilt angles are acquired and merged into a 3D tomogram [60]. From multiple tomograms, sub-volumes around the helices are excised, aligned by applying cylindrical restraints and averaged without imposing any symmetry [61]. Once the aligned positions of the sub-volumes

are traced back into the original tomogram, they directly represent the unit positions within the helical lattice and low-resolution symmetry parameters are obtained (Figure 7). In addition, this method reveals symmetry heterogeneity between different helices in the same sample as recently described for clathrin adaptors ANTH-ENTH tubules that possess a wide range of different helical arrangements [62]. Another advantage of this approach is that the obtained tomograms also display deformations of wide helical tubes when they are significantly compressed in the ice layer. Such distortions are very difficult to detect in projection images alone whereas tomograms reveal such imperfections and thus the affected helices can be excluded from further processing [63]. Subsequently, it is useful to further refine the obtained symmetry parameters and compute high-resolution structures based on high-dose projection images as outlined below. While sub-volume averaging may have limitations for smaller helical units where the signal is not sufficient for reliable alignment it has the future potential to overcome many of the inherent problems that arise from interpreting helical projection images.

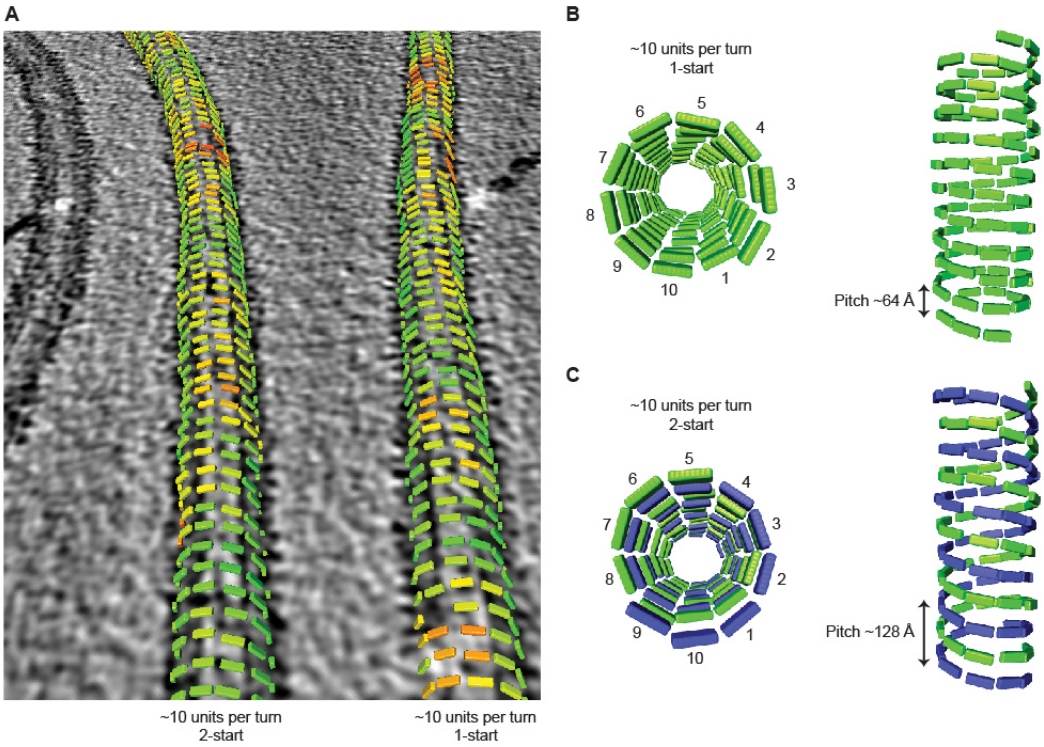

Figure 7. Example of real-space symmetry determination using sub-volume averaging. Clathrin adaptors ANTH and ENTH form helical co-assemblies on lipid tubules. Tracing the positions of the sub-volumes after alignment reveals the helical lattice. In this tomogram, two tubules have approximately 10 subunits per turn and are arranged in 1- and 2-start helices. The color of rectangles corresponds to the cross-correlation value of each subtomogram with the reference from high (green) to low (red). Reproduced from Skruzny et al., 2015 [62]**.**

1.6. Complementary information on helical symmetry

As mentioned above the *de novo* interpretation of Fourier spectra remains one of the challenges

for helical structure determination. Therefore complementary experimental data can restrain the number of solutions that are ambiguous or similar. One possibility presents scanning transmission electron microscopy (STEM), which provides mass measurements of biomolecules [64]. In the presence of the helical reference TMV, samples are freeze-dried and subjected to STEM imaging. By calibrating the image intensity of the target helix to the reference TMV mass-per-length measures in kDa/nm can be obtained [65]. Such measurements limit the number of possible indexing schemes significantly and provide independent experimental validation. It should be noted that the Brookhaven National Laboratory is currently the only institution worldwide offering a service to perform such measurements.

As projections recorded in the electron microscope contain mass contributions through the entire object, it is impossible to discriminate top and bottom contributions of the helix, which means that no information on the handedness of the assembly is available. This limitation can be overcome if the helix is subjected to shadowing to coat the helical surface with a fine metal grain [66]. In exceptional cases, freeze drying followed by unidirectional Tungsten/Tantalum (W/Ta) shadowing in the electron microscope can reveal such a detailed helix surface topography to determine the helical lattice of tubulin sheets and microtubules [67]. Fine and coarse grain shadowing for helical specimens is still useful to determine the handedness of helices. If low-resolution features like pitch are not obscured by the coarse metal grain, the images reveal the surface orientation of those features and therefore provide the hand of the helix [59]. Similarly, atomic force microscopy (AFM) can provide such information [68]. Tilting low-pitch helices out of the plane can also identify the hand as it reveals a characteristic superposition pattern on the left or right-hand side of the helix projection [69] (Figure 6G). In addition, electron tomography and sub-volume averaging can give the correct hand of the imaged helix if the acquisition and processing workflow has been calibrated with the hand of a reference specimen. The determination of the hand of the helix is relevant for cases where interpretation with atomic models is not possible or ambiguous. Once the resolution exceeds beyond 1 nanometer and subunits can be reliably fitted based on their fold, only the EM density with the correct hand can be fitted with the atomic coordinates. For *de novo* atomic model building high-resolution structural features such as α-helical pitch will provide the correct hand of the overall helical assembly.

1.7. Symmetry refinement

Once the helical indexing of layer lines has been successful and the helical lattice including the hand has been derived, the symmetry parameters need to be refined for high-resolution analysis as all of the described methods rely on low-resolution analysis. In single-particle helical reconstruction algorithms two main approaches are being used. First, the iterative helical real-space reconstruction (IHRSR) method refines the helical symmetry by fitting helical densities in an asymmetric reconstruction that has no symmetry imposed [26]. At the end of each iteration cycle, the updated symmetry parameters are used to impose helical symmetry on the 3D structure and another projection matching cycle is launched. This way the helical symmetry values finally converge over many cycles. The second method involves many parallel reconstructions over a grid of symmetry combinations and finally evaluates those independently using power spectra matching [27,70]. Experimental power spectra are obtained from in-plane rotated segments that have not been subjected to any 3D parameter search. These Fourier spectra have the advantage that they can be

averaged over large data sets while they are not biased to match any reference, which is one of the major problems in reference-based alignment procedures with low-signal EM images [71]. The experimental power spectra are now compared with power spectra from re-projections of the 3D reconstructions from refinements of the symmetry grid (Figure 2C). For each of the symmetry grid points, the best matching spectra can be diagnosed and finer grids may be searched in case the high-resolution layer lines do not match satisfactorily yet. Such power spectra comparisons yield resolution-dependent amplitude correlation values that can be iteratively maximized and provide diagnostics for validation of the symmetry search.

1.8. High-resolution helical reconstruction

Once the symmetry parameters have been refined, high-resolution reconstruction can be performed (Figure 2D). With the advent of DDDs near-atomic resolution of many helical structures has become within reach provided the assemblies are well ordered. Segments of helices contain a significant molecular mass that provides sufficient signal intensity for reliable alignment. One of the first indicators of how well a 3D structure can be potentially resolved can be estimated from the sum of overlapping Fourier spectra generated as described above. Analyzing Fourier spectra of many helices has the advantage over selecting individual helices that high-resolution layer lines may also become visible after averaging. Additional averaging can be obtained by computing collapsed power spectra profiles that are averaged along the layer lines. In the case of TMV images recorded on direct electron detectors, we found that the sum of the collapsed power spectra revealed layer lines at 3.3 Å that corresponded to the final resolution of the reconstruction [24] (Figure 8). An essential step to recover such high-resolution frequencies in the 3D reconstruction is the correction of CTF induced by acquiring micrographs under focus. The microscope parameters are determined using CTFFIND or CTFTILT software [72]. Un updated CTFFIND4 version is now available optimized for defocus determination from DDD micrographs (http://grigoriefflab.janelia.org). An efficient way to correct the CTF is achieved by convolving the helical segments with a CTF [13,41,73,74]. In effect, the phases are corrected and amplitudes are weighted according to the expected signal from the theoretical CTF function. After combining all convolved images into the 3D reconstruction, the resulting volume contains modified amplitudes that correspond to an average of CTF^2 from all segments. In order to correct these amplitudes, the average of CTF^2 from all segments is computed independently and the 3D reconstruction is divided by that average CTF^2 including a constant resulting in an operation that is equivalent to a Wiener filter.

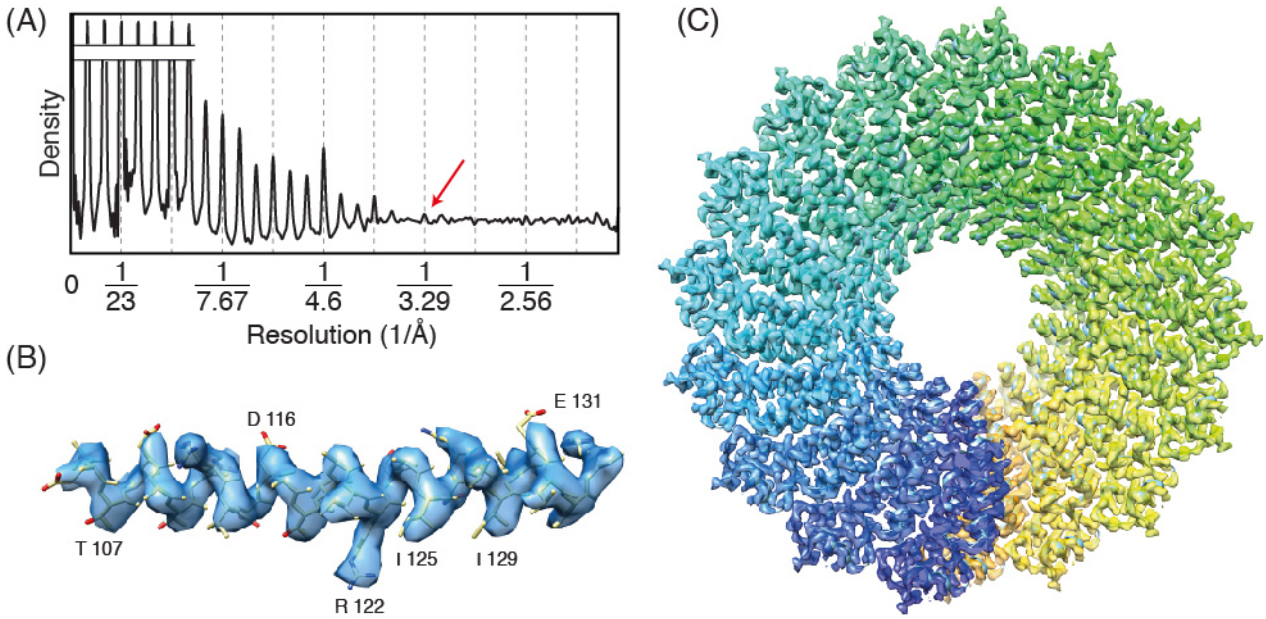

Figure 8. Atomic-resolution structure of TMV computed from direct electron detector images (Fromm et al., 2015). (A) Collapsed amplitude spectrum with layer-line peaks up to 3.3 Å obtained from the sum of the power spectra of helical segments. (B) Example of a 3.35 Å cryo-EM density from long α-helix T107-E131. (C) Top view of 17 subunits that make up a complete turn in helical tobacco mosaic virus.

The basic workflow of single-particle based helical reconstruction (Figure 2D) follows the common projection matching routine [11]. Low-resolution models like a cylinder or class-based reconstructions are suitable as initial models. Once the correct helical symmetry is applied the radius of convergence of the algorithm is small. Reprojections of those models are generated around the helical axis to yield unique azimuthal views [26]. In addition, out-of-plane tilt for rigid specimens ±12º or for more flexible helices up to ±20º should be considered for high-resolution analysis. Subsequently, all CTF convolved images keep their original in-plane rotation from the micrograph and are being multiplied by a rectangular mask. The images are matched against the generated projections in a procedure, which corresponds to a 5-parameter search of the x, y position and the 3 Euler angles. Once segmentation has been applied to the helices, the information on the connectivity between segments is lost. It is, however, very useful to analyze the determined alignment parameters on the basis of a continuous helix. For example, if segment polarity is tracked over a continuous helix, oppositely aligned segments from the majority of the segments belonging to that helix can be discarded from the reconstruction. Furthermore, the average shift perpendicular to the helix should be continuous along a helix. Deviation from such a continuous shift can be interpreted as alignment error [13]. When simply applying these selection criteria they give useful statistics on the validity and precision of the refinement procedure that pure single-particle analysis cannot provide. A recent application takes this basic approach further, to build a continuous helical presentation such that all segments of a helix are aligned simultaneously while applying continuity restraints [28]. This procedure has the potential to deal with very flexible filaments such as amyloid fibrils. Once segments are selected and alignment parameters applied, they will be combined into a 3D volume

using the orientation parameters. Symmetrization is an integral part of the 3D reconstruction by supplying symmetry-equivalent views to the reconstruction algorithm. In order to maximize signal over noise the 3D reconstruction is computed from the total number of asymmetric units present in the helical projections [13,27].

Currently, multiple software solutions exist to reconstruct helices. According to the EMDB entries, many structures were solved by using a combination of software with approximately 1/4 of structures using Fourier-based reconstruction methods, while 3/4 using single-particle approaches (Figure 9). While traditionally, helical processing was performed in Fourier space, the success of the iterative helical real-space reconstruction (IHRSR) method [26] inspired numerous packages to adapt single-particle processing to helical specimens. Packages that are traditionally known as single-particle software such as FREALIGN, SPARX, BSOFT [25,75,76] have released workflows suitable for the 3D reconstruction of helical assemblies. RELION a package that applies Bayesian statistics to single-particle structure refinement [77] has recently been modified for specimens of helical symmetry [78]. A more recent development is represented by the SPRING package, which combines many of the tools required for the Fourier domain analysis outlined above and real-space high-resolution 3D reconstruction into one unique workflow [27]. For example, Fourier analysis of class averages can provide important structural parameters of the helix and can be used to compute initial reconstructions to assess the helical symmetry. Using this package, EM images from well-preserved helical assemblies such as ParM filaments and Measles virus have produced near-atomic resolution structures [22,79] but also more flexible and heterogeneous helices such as PB1 domains from autophagy receptor p62/SQSTM1 and lipid tubular co-assemblies of clathrin adaptors ANTH-ENTH have been determined at intermediate resolution [62,80]. Moreover, SPRING has been adapted to process movies recorded with DDDs [24].

In the past two years, the introduction of DDDs triggered a leap forward in the number of releases and the quality of high-resolution cryo-EM structures [81]. Such devices provide a major boost in signal-to-noise ratio of micrographs in particular for high-resolution frequencies [82]. A number of near-atomic resolution structures are available, from asymmetric to lower and higher point group symmetries as well as helical symmetries taken on various DDDs [17,19,83–86]. The large mass and high stability of helical specimens such as TMV make them ideal test specimens to characterize the performance of a selection of commercial DDD cameras [24] all of which are capable of producing 4 Å resolution reconstructions with as little as 11,000 asymmetric units. Fast read-out rates of the new generation of cameras enable tracking of beam-induced movement in movie frames [87]. Thus, micrographs are corrected for movement during imaging and significantly improve information transfer [19]. Particle-based motion tracking has been successful for large assemblies [84] but can be limiting for smaller particles due the reduced signal available in the frames. Therefore, additional running averages of frames or local averaging of particles in micrograph areas have been included as approaches to keep increasing alignment errors small [88]. Such an approach will also be applicable to helical assemblies where local averaging of motion along helices prevents increasing alignment errors for frames with little signal and dose. On a traditional micrograph recorded at 300 kV acceleration voltage, an exposure of 15 to 25 $e^-/Å^2$ were previously used to determine the 3D structure. More recently, it became clear that in order to preserve resolutions beyond 4 Å dose limitation to 20 $e^-/Å^2$ or significant down-weighting of the later image frames is essential to minimize the effects of radiation damage [19,83,88]. The new hardware of DDDs helped to better characterize the details of the imaging process in cryo-EM and combined with additional processing

strategies it helped to increase information content that can be extracted from cryo-EM images.

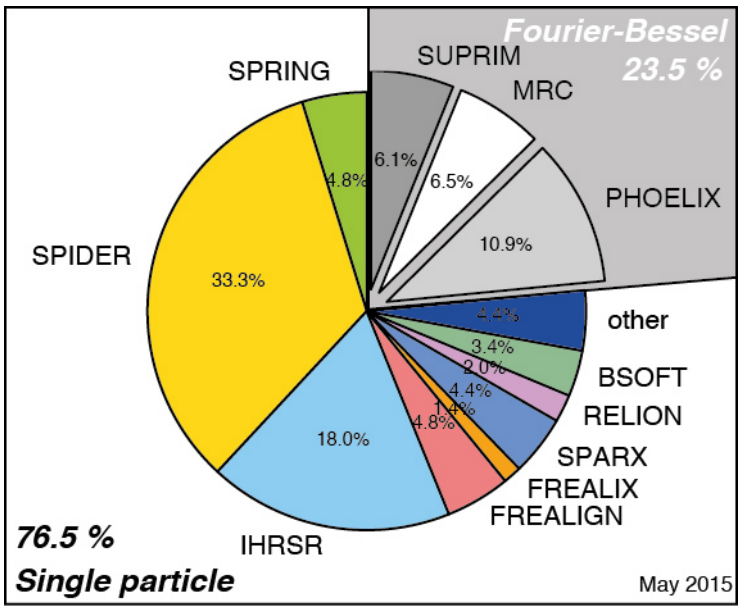

Figure 9. Comparison of software packages using Fourier and single-particle based helical image reconstructions. Pie chart of software entries from the EM databank used for processing of helical assemblies. Traditionally, helical image reconstruction was developed using Fourier-Bessel analysis that were used in approximately 24 % of all helical entries. Single-particle based software now represent the most commonly used approaches for 3D reconstruction of helical specimens. In many cases, multiple software suites were used for a single EMDB entry to validate the determined helical structure.

2. Conclusion

Macromolecular helices remain important and highly interesting assemblies to be studied. They include molecules of the cytoskeleton, signaling complexes, pathological aggregate types and many others involved in essential biological processes. Helical assemblies have significantly contributed to characterization, development and advancement of structure determination methods [1,13,52,89] as they can provide rigid and highly organized assemblies. For example, TMV rafts when imaged in the electron microscope using diffraction mode revealed layer lines to up to 2.3 Å [90]. Currently, images taken from well-ordered TMV using direct electron detectors did not capture measureable layer line data beyond 3.2 Å in resolution [24]. In the meantime, recent studies on β-galactosidase and rotavirus VP6 demonstrated that resolutions at 2.3 and 2.6 Å have become possible by singe-particle cryo-EM from micrographs taken on DDD cameras [91,92]. It is clear that more research is needed to extract the highest resolution from cryo-EM images. Test specimens such as helical TMV may play an important role in this process. In addition, many other helical specimens have not yet been discovered and still await structural elucidation. For *de novo* helical structure determination, resolving the helical lattice parameters remains one of the major challenges. Due to the complexity involved in interpreting Fourier spectra and real-space images one of the important

questions that remains to be addressed is whether helical parameters can be extracted in an automated or semi-automated indexing procedure. Although many of the recent near-atomic resolution structures came from specimens that have been studied for decades [22,23,40,41,79], there is good reason to believe that many entirely unknown helical assemblies can be resolved at similar accuracy. A combination of hardware and software-based improvements [13,19,25–27,93] have made helical assemblies a very productive field of research that continues to thrive.

Acknowledgments

SPRING—one of the abovementioned software packages that integrates Fourier and real-space methods is available from the author's website (http://www.sachse.embl.de/emspring). Figures 4, 5 and 6 were generated using the programs SEGLAYER2LATTICE and SEGCLASSLAYER from the SPRING software suite. I would like to thank Simon Fromm for preparing Figure 8 of the high-resolution TMV reconstruction. I am grateful to Ambroise Desfosses for numerous helpful discussions and comments on the manuscript. I thank John Briggs and Peter Rosenthal for critically reading the manuscript.

Conflict of Interest

The author declares no conflict of interest.

References

1. De Rosier D, Klug A (1968) Reconstruction of Three Dimensional Structures from Electron Micrographs. *Nature* 217: 130–134.
2. Cochran W, Crick FHC, Vand V (1952) The Structure of Synthetic Polypeptides. I. The Transform of Atoms on a Helix. *Acta Crystallographica* 5: 581–586.
3. Franklin RE, Klug A (1955) The splitting of layer lines in X-ray fibre diagrams of helical structures: application to tobacco mosaic virus. *Acta Crystallographica* 8: 777–780.
4. Franklin R, Holmes K (1958) Tobacco mosaic virus: application of the method of isomorphous replacement to the determination of the helical parameters and radial density distribution. *Acta Crystallographica* 11: 213–220.
5. Crowther RA, Amos LA, Finch JT, et al. (1970) Three dimensional reconstructions of spherical viruses by fourier synthesis from electron micrographs. *Nature* 226: 421–425.
6. Adrian M, Dubochet J, Lepault J, et al. (1984) Cryo-electron microscopy of viruses. *Nature* 308: 32–36.
7. Henderson R, Baldwin JM, Ceska TA, et al. (1990) Model for the structure of bacteriorhodopsin based on high-resolution electron cryo-microscopy. *J Mol Biol* 213: 899–929.
8. Miyazawa A, Fujiyoshi Y, Unwin N. (2003) Structure and gating mechanism of the acetylcholine receptor pore. *Nature* 423: 949–955.
9. Yonekura K, Maki-Yonekura S, Namba K (2003) Complete atomic model of the bacterial flagellar filament by electron cryomicroscopy. *Nature* 424: 643–650.
10. van Heel M, Frank J (1981) Use of multivariate statistics in analysing the images of biological macromolecules. *Ultramicroscopy* 6: 187–194.

11. Penczek PA, Grassucci RA, Frank J (1994) The ribosome at improved resolution: new techniques for merging and orientation refinement in 3D cryo-electron microscopy of biological particles. *Ultramicroscopy* 53: 251–270.
12. Lawson CL, Baker ML, Best C, et al. (2011) EMDataBank.org: unified data resource for CryoEM. *Nucleic Acids Res* 39: D456–64.
13. Sachse C, Chen JZ, Coureux P-D, et al. (2007) High-resolution electron microscopy of helical specimens: a fresh look at tobacco mosaic virus. *J Mol Biol* 371: 812–835.
14. Yu X, Jin L, Zhou ZH (2008) 3.88 A structure of cytoplasmic polyhedrosis virus by cryo-electron microscopy. *Nature* 453: 415–419.
15. Zhang X, Settembre E, Xu C, et al. (2008) Near-atomic resolution using electron cryomicroscopy and single-particle reconstruction. *Proc Natl Acad Sci USA* 105: 1867–1872.
16. Cong Y, Baker ML, Jakana J, et al. (2010) 4.0-A resolution cryo-EM structure of the mammalian chaperonin TRiC/CCT reveals its unique subunit arrangement. *Proc Natl Acad Sci USA* 107: 4967–4972.
17. Bai X-C, Fernandez IS, McMullan G, et al. (2013) Ribosome structures to near-atomic resolution from thirty thousand cryo-EM particles. *eLife* 2: e00461.
18. Voorhees RM, Fernandez IS, Scheres SHW, et al. (2014) Structure of the Mammalian ribosome-sec61 complex to 3.4 å resolution. *Cell* 157: 1632–1643.
19. Li X, Mooney P, Zheng S, et al. (2013) Electron counting and beam-induced motion correction enable near-atomic-resolution single-particle cryo-EM. *Nat Methods* 10: 584–590.
20. Lu P, Bai X-C, Ma D, et al. (2014) Three-dimensional structure of human γ-secretase. *Nature* 512: 166–170.
21. Wu B, Peisley A, Tetrault D, et al. (2014) Molecular imprinting as a signal-activation mechanism of the viral RNA sensor RIG-I. *Mol Cell* 55: 511–523.
22. Bharat TAM, Murshudov GN, Sachse C, et al. (2015) Structures of actin-like ParM filaments show architecture of plasmid-segregating spindles. *Nature*: 1–5.
23. Ecken von der J, Müller M, Lehman W, et al. (2015) Structure of the F-actin-tropomyosin complex. *Nature* 519: 114–117.
24. Fromm SA, Bharat TAM, Jakobi AJ, et al. (2015) Seeing tobacco mosaic virus through direct electron detectors. *J Struct Biol* 189: 87–97.
25. Behrmann E, Tao G, Stokes DL, et al. (2012) Real-space processing of helical filaments in SPARX. *J Struct Biol*: 1–12.
26. Egelman EH (2000) A robust algorithm for the reconstruction of helical filaments using single-particle methods. *Ultramicroscopy* 85: 225–234.
27. Desfosses A, Ciuffa R, Gutsche I, et al. (2014) SPRING—an image processing package for single-particle based helical reconstruction from electron cryomicrographs. *J Struct Biol* 185: 15–26.
28. Rohou A, Grigorieff N (2014) Frealix: model-based refinement of helical filament structures from electron micrographs. *J Struct Biol* 186: 234–244.
29. Sindelar CV, Downing KH (2007) The beginning of kinesin's force-generating cycle visualized at 9-A resolution. *J Cell Biol* 177: 377–385.
30. Klug A, Crick FHC, Wyckhoff HW (1958) Diffraction by Helical Structures. *Acta Crystallographica* 11: 199–213.

31. Caspar DL, Klug A (1962) Physical principles in the construction of regular viruses. *Cold Spring Harb Symp Quant Biol* 27: 1–24.
32. Moore PB, Huxley HE, DeRosier DJ (1970) Three-dimensional reconstruction of F-actin, thin filaments and decorated thin filaments. *J Mol Biol* 50: 279–295.
33. Mandelkow EM, Mandelkow E (1985) Unstained microtubules studied by cryo-electron microscopy. Substructure, supertwist and disassembly. *J Mol Biol* 181: 123–135.
34. Finch JT (1964) Resolution of the substructure of tobacco mosaic virus in the electron microscope. *J Mol Biol* 8: 872–874.
35. Sachse C, Fändrich M, Grigorieff N (2008) Paired beta-sheet structure of an Abeta(1-40) amyloid fibril revealed by electron microscopy. *Proc Natl Acad Sci USA* 105: 7462–7466.
36. Carragher B, Bluemke DA, Gabriel B, et al. (1988) Structural analysis of polymers of sickle cell hemoglobin. I. Sickle hemoglobin fibers. *J Mol Biol* 199: 315–331.
37. Xu C, Rice WJ, He W, et al. (2002) A structural model for the catalytic cycle of Ca(2+)-ATPase. *J Mol Biol* 316: 201–211.
38. Korkhov VM, Sachse C, Short JM, et al. (2010) Three-dimensional structure of TspO by electron cryomicroscopy of helical crystals. *Structure* 18: 677–687.
39. Hou F, Sun L, Zheng H, et al. (2011) MAVS forms functional prion-like aggregates to activate and propagate antiviral innate immune response. *Cell* 146: 448–461.
40. Alushin GM, Lander GC, Kellogg EH, et al. (2014) High-Resolution Microtubule Structures Reveal the Structural Transitionsin ab-Tubulin upon GTP Hydrolysis. *Cell* 157: 1117–1129.
41. Galkin VE, Orlova A, Vos MR, et al. (2015) Near-atomic resolution for one state of f-actin. *Structure* 23: 173–182.
42. Stewart M (1988) Computer image processing of electron micrographs of biological structures with helical symmetry. *J Electron Microsc Tech* 9: 325–358.
43. DeRosier DJ, Moore PB (1970) Reconstruction of three-dimensional images from electron micrographs of structures with helical symmetry. *J Mol Biol* 52: 355–369.
44. Moody MF (1990) Biophysical electron microscopy: basic concepts and modern techniques—image analysis of electron micrographs. 517.
45. Carragher B, Whittaker M, Milligan RA (1996) Helical processing using PHOELIX. *J Struct Biol* 116: 107–112.
46. Owen CH, Morgan DG, DeRosier DJ (1996) Image analysis of helical objects: the Brandeis Helical Package. *J Struct Biol* 116: 167–175.
47. Beroukhim R, Unwin N (1997) Distortion correction of tubular crystals: improvements in the acetylcholine receptor structure. *Ultramicroscopy* 70: 57–81.
48. Pomfret AJ, Rice WJ, Stokes DL (2007) Application of the iterative helical real-space reconstruction method to large membranous tubular crystals of P-type ATPases. *J Struct Biol* 157: 106–116.
49. Ramey VH, Wang H-W, Nogales E (2009) Ab initio reconstruction of helical samples with heterogeneity, disorder and coexisting symmetries. *J Struct Biol* 167: 97–105.
50. Diaz R, Rice WJ, Stokes DL. (2010) Fourier-Bessel reconstruction of helical assemblies. *Meth Enzymol* 482: 131–165.
51. Erickson HP, Klug A (1971) Measurement and Compensation of Defocusing and Aberrations by Fourier Processing of Electron Micrographs. *Philos Trans R Soc Lond, B, Biol Sci* 261: 105–118.

52. Henderson R (1992) Image contrast in high-resolution electron microscopy of biological macromolecules: TMV in ice. *Ultramicroscopy* 46: 1–18.
53. Glaeser RM (2007) *Electron Crystallography of Helical Structures in Electron Crystallography of Biological Macromolecules*. Oxford University Press, USA; 2007: 304–342.
54. Egelman EH (2010) Reconstruction of helical filaments and tubes. *Meth Enzymol* 482: 167–183.
55. Heymann JB, Chagoyen M, Belnap DM (2005) Common conventions for interchange and archiving of three-dimensional electron microscopy information in structural biology. *J Struct Biol* 151:196–207.
56. Egelman EH (2014) Ambiguities in helical reconstruction. *eLife* 3.
57. Vonck J (2000) Parameters affecting specimen flatness of two-dimensional crystals for electron crystallography. *Ultramicroscopy* 85: 123–129.
58. Moody MF (2011) *Structural Biology Using Electrons and X-Rays*. Academic Press; 2011.
59. Sachse C, Xu C, Wieligmann K, et al. (2006) Quaternary structure of a mature amyloid fibril from Alzheimer's Abeta(1-40) peptide. *J Mol Biol* 362: 347–354.
60. Lučić V, Förster F, Baumeister W (2005) STRUCTURAL STUDIES BY ELECTRON TOMOGRAPHY: From Cells to Molecules. *Annu Rev Biochem* 74: 833–865.
61. Briggs JA (2013) Structural biology in situ—the potential of subtomogram averaging. *Curr Opin Struct Biol* 23: 261–267.
62. Skruzny M, Desfosses A, Prinz S, et al. (2015) An Organized Co-assembly of Clathrin Adaptors Is Essential for Endocytosis. *Dev Cell* 33: 150–162.
63. Bharat TAM, Davey NE, Ulbrich P, et al. (2012) Structure of the immature retroviral capsid at 8 Å resolution by cryo-electron microscopy. *Nature* 487: 385–389.
64. Wall JS, Hainfeld JF (1986) Mass mapping with the scanning transmission electron microscope. *Annu Rev Biophys Biophys Chem* 15: 355–376.
65. Wall JS, Simon MN (2001) Scanning transmission electron microscopy of DNA-protein complexes. *Methods Mol Biol* 148: 589–601.
66. Scheele RB, Borisy GG (1978) Electron microscopy of metal-shadowed and negatively stained microtubule protein. Structure of the 30 S oligomer. *J Biol Chem* 253: 2846–2851.
67. Hoenger A, Doerhoefer M, Woehlke G, et al. (2000) Surface topography of microtubule walls decorated with monomeric and dimeric kinesin constructs. *Biol Chem* 381: 1001–1011.
68. Schmitz S, Schaap IAT, Kleinjung J, et al. (2010) Malaria Parasite Actin Polymerization and Filament Structure. *J Biol Chem* 285: 36577–36585.
69. Finch JT (1972) The hand of the helix of tobacco virus. *J Mol Biol* 66: 291–294.
70. Low HH, Sachse C, Amos LA, et al. (2009) Structure of a bacterial dynamin-like protein lipid tube provides a mechanism for assembly and membrane curving. *Cell* 139: 1342–1352.
71. Stewart A, Grigorieff N (2004) Noise bias in the refinement of structures derived from single particles. *Ultramicroscopy* 102: 67–84.
72. Mindell JA, Grigorieff N (2003) Accurate determination of local defocus and specimen tilt in electron microscopy. *J Struct Biol* 142: 334–347.
73. Grigorieff N (1998) Three-dimensional structure of bovine NADH:ubiquinone oxidoreductase (complex I) at 22 A in ice. *J Mol Biol* 277: 1033–1046.
74. Fujii T, Iwane AH, Yanagida T, et al. (2010) Direct visualization of secondary structures of F-actin by electron cryomicroscopy. *Nature* 467: 724–728.

75. Grigorieff N (2007) FREALIGN: high-resolution refinement of single particle structures. *J Struct Biol* 157: 117–125.
76. Heymann JB, Belnap DM (2007) Bsoft: image processing and molecular modeling for electron microscopy. *J Struct Biol* 157: 3–18.
77. Scheres SHW (2012) RELION: Implementation of a Bayesian approach to cryo-EM structure determination. *J Struct Biol* 180: 519–530.
78. Clemens DL, Ge P, Lee B-Y, et al. (2015) Atomic Structure of T6SS Reveals Interlaced Array Essential to Function. *Cell* 160: 940–951.
79. Gutsche I, Desfosses A, Effantin G, et al. (2015) Structural virology. Near-atomic cryo-EM structure of the helical measles virus nucleocapsid. *Science* 348: 704–707.
80. Ciuffa R, Lamark T, Tarafder AK, et al. (2015) The Selective Autophagy Receptor p62 Forms a Flexible Filamentous Helical Scaffold. *Cell Rep* 11: 748–758.
81. Kühlbrandt W (2014) The Resolution Revolution. *Science* 343: 1443–1444.
82. Faruqi AR, Henderson R (2007) Electronic detectors for electron microscopy. *Curr Opin Struct Biol* 17: 549–555.
83. Wang Z, Hryc CF, Bammes B, et al. (2014) An atomic model of brome mosaic virus using direct electron detection and real-space optimization. *Nat Commun* 5: 4808.
84. Campbell MG, Cheng A, Brilot AF, et al. (2012) Movies of ice-embedded particles enhance resolution in electron cryo-microscopy. *Structure* 20: 1823–1828.
85. Bartesaghi A, Matthies D, Banerjee S, et al. (2014) Structure of β-galactosidase at 3.2-Å resolution obtained by cryo-electron microscopy. *Proc Natl Acad Sci USA* 111: 11709–11714.
86. Allegretti M, Mills DJ, McMullan G, et al. (2014) Atomic model of the F420-reducing [NiFe] hydrogenase by electron cryo-microscopy using a direct electron detector. *eLife* 3: e01963–e01963.
87. Brilot AF, Chen JZ, Cheng A, et al. (2012) Beam-induced motion of vitrified specimen on holey carbon film. *J Struct Biol* 177: 630–637.
88. Scheres SH (2014) Beam-induced motion correction for sub-megadalton cryo-EM particles. *eLife* 3: e03665.
89. Holmes K, Franklin R (1958) The radial density distribution in some strains of tobacco mosaic virus. *Virology* 6: 328–336.
90. Cyrklaff M, Kühlbrandt W (1994) High-resolution electron microscopy of biological specimens in cubic ice. *Ultramicroscopy* 55: 141–153.
91. Grant T, Grigorieff N (2015) Measuring the optimal exposure for single particle cryo-EM using a 2.6 Å reconstruction of rotavirus VP6. *eLife* 4.
92. Bartesaghi A, Merk A, Banerjee S, et al. (2015) Electron microscopy. 2.2 Å resolution cryo-EM structure of β-galactosidase in complex with a cell-permeant inhibitor. *Science* 348: 1147–1151.
93. McMullan G, Faruqi AR, Henderson R, et al. (2009) Experimental observation of the improvement in MTF from backthinning a CMOS direct electron detector. *Ultramicroscopy* 109: 1144–1147.

© 2015, Carsten Sachse, licensee AIMS Press. This is an open access article distributed under the terms of the Creative Commons Attribution License (http://creativecommons.org/licenses/by/4.0)